Contents of this file

S1 Perimeter density

In this study, we use the perimeter density per unit ice area P (units: km km^{-2}) to evaluate the model performance, as it reduces the impacts of partially captured floes at the edge of the image for the FSD retrieval (Perovich, 2002; Perovich and Jones, 2014). There are a number of ways to calculate P. In the following, we describe how the FSD models calculate P, as well as how P can be calculated from the observational FSD data.

Calculation of P in the FSD models

In FSD models, P is calculated from number FSD n_i distributed into floe size categories i as follows:

$$P = \frac{\sum_{i=1}^{12}(2\gamma r_i n_i w_i)}{c_{ice}}, \quad \text{(S1)}$$

where r_i and w_i are the midpoint and bin width for each floe size category i. n_i (m^{-3}) is the number of floes in floe size category i per unit bin width per unit area So $n_i w_i$ is the number of floes per unit area for each floe size category i. The upper term in the right hand of Eq. S1 is the perimeter of floes per unit area. By dividing total floe perimeter per unit ocean area by the sea-ice concentration, c_{ice}, we obtain the total floe perimeter per unit sea ice area.

The floe fractional-area distribution $f(r)dr$ and floe number-density distribution $n(r)dr$ are related by

$$\int_{r_0}^{\infty} f(r)dr = \int_{r_0}^{\infty} \pi r^2 n(r)dr, \quad \text{(S2)}$$

where r_0 is the lowest cut-off of floe size r. By combining Eqs. S1–S2, P for prognostic model P_{prog} can be calculated as Eq. 2 in the main text.

For WIPoFSD model, a truncated power law FSD is applied,

$$n(r|r_{min} \le r \le r_{var}) = cr^{-\alpha}, \quad \text{(S3)}$$

where, r_{min} is the minimum floe radius within floe size categories. The power-law exponent α value used in this study is set to 2.56. The floe size parameter r_{var} varies between r_{min} and the maximum floe radius r_{max} in response to four FSD evolution processes described by Bateson et al. (2020, 2022). The normalization constant c can be defined from that the integral of areal FSD over all floe sizes equal to the fraction of sea ice,

$$\pi \int_{r_{min}}^{r_{var}} n(r)r^2 dr = c_{ice} \quad \text{(S4)}$$

$$\text{Hence } c = \frac{(3-\alpha)c_{ice}}{(r_{var}{}^{3-\alpha} - r_{min}{}^{3-\alpha})\pi} \quad \text{(S5)}$$

Perimeter density for WIPoFSD, $P_{wipofsd}$, can be calculated from Eqs. S1, S3 and S5 (see Eq. 2 in the main text).

Calculation of P from the observations

To ensure matching with the model outputs, the FSD observation data were binned into the same 12 floe size categories used by the FSD models (Gaussian spacing). By deriving the number of all floes with effective floe radius $r = \sqrt{\frac{a}{\pi}}$ (Horvat and Tziperman, 2015), the radius of a circle that has the same area as a floe, within every floe size category, the average number FSD for each floe size category n_i can be calculated by

$$n_i = \frac{N_i}{A_{ocean} w_i}, \tag{S6}$$

where N_i is the number of floes with radius between $r_{i_{min}}$ and $r_{i_{max}}$ in the image covering an ocean area of A_{ocean} (units: m2) with floe radius between $r_{i_{min}}$ and $r_{i_{max}}$.

Similarly, the average areal FSD for floe size category f_i can be calculated by

$$f_i = \frac{A_{floe_i}}{A_{ocean} w_i}. \tag{S7}$$

A_{floe_i} is the area of floes with radius between $r_{i_{min}}$ and $r_{i_{max}}$ in the image.

Now based on the equations described above, we can calculate P from the observations using three different methods. From Eqs. S2 and S6, we can produce perimeter density per unit sea ice area from observations using the number FSD,

$$P_{obs1} = \frac{\sum_{i=1}^{12}(2\gamma r_i N_i)}{A_{ice}}, \tag{S8}$$

where A_{ice} is the total area of sea ice within the image.

Based on Eq. 2 in the main text and Eq. S7 shown above, the perimeter density can be calculated by,

$$P_{obs2} = \sum_{i=1}^{12} \frac{2\gamma A_{floe_i}}{\pi r_i A_{ice}}. \tag{S9}$$

Additionally, we can calculate the floe perimeter density directly from our images,

$$P_{obs3} = \frac{p_{floe}(r_{1_{min}} < r < r_{12_{max}})}{A_{ice}}, \tag{S10}$$

where p_{floe} is the total perimeter of floes with radius between $r_{1_{min}}$ and $r_{12_{max}}$ in the image. In Sect. S2, we will test the sensitivity of calculating the perimeter density using Eqs. S8–S10.

S2 Sensitivity to the floe size category binning and *P* calculation methods.

In this section, we check the sensitivity of calculating P for different binning methods and different P calculation methods (Eqs. S8–S10 in Sect. S1). To test the sensitivity of the binning methods, we organised the observational FSD data into four different binning methods: 12 Gaussian-spaced bins, 24 Gaussian-spaced bins, 12 evenly spaced bins, and 24 evenly spaced bins. For the binning, we discarded any ice floes with the effective radius smaller than 0.1 m or larger than 951 m.

Figure S1 shows the results in the relationship between P and SIC. As can be seen in Figure S1, the P values from evenly spaced binning methods are very sensitive to the different P calculation methods (Figure S1c and d). On the other hand, the P

values from Gaussian spaced binning methods are much less sensitive to the different P calculation methods and there are very small differences in the sensitivities between 12 Gaussian spaced binned data and 24 Gaussian spaced binned data (Figure S1a and S1b). Among the three different P calculation methods, P_{obs2} (Eq. S9, estimated using the floe area) shows the smallest variation throughout the four different binning methods. Based on this, we selected P_{obs2} to calculate P and use it as the metric for the model-observation comparison and the 12 Gaussian-spaced binning method to match with the model configuration in Roach et al. (2018a) and Bateson et al. (2022).

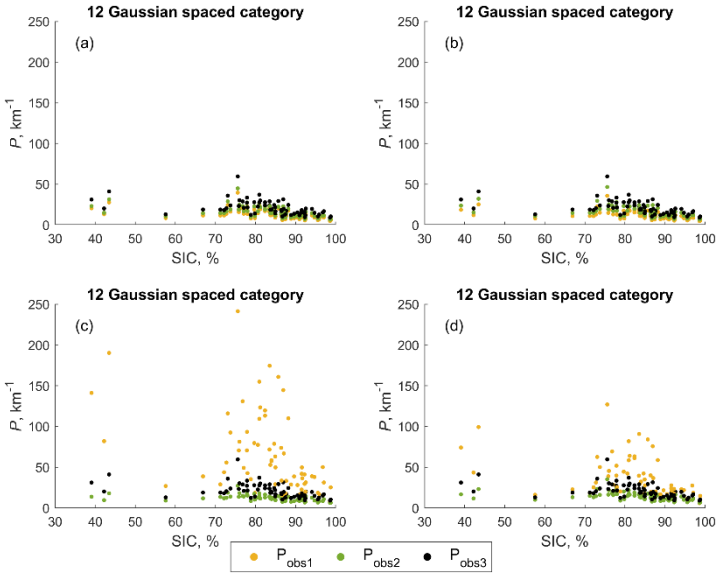

Figure S1. Relationship between perimeter density per unit ice area and SIC for (a) 12 Gaussian-spaced binning, (b) 24 Gaussian-spaced binning, (c) 12 evenly spaced binning, and (d) 24 evenly spaced binning. The perimeter density has been calculated using Eq. S8 (P_{obs1}, yellow scatter), Eq. S9 (P_{obs2}, green scatter) and Eq. S10 (P_{obs3}, black scatter).

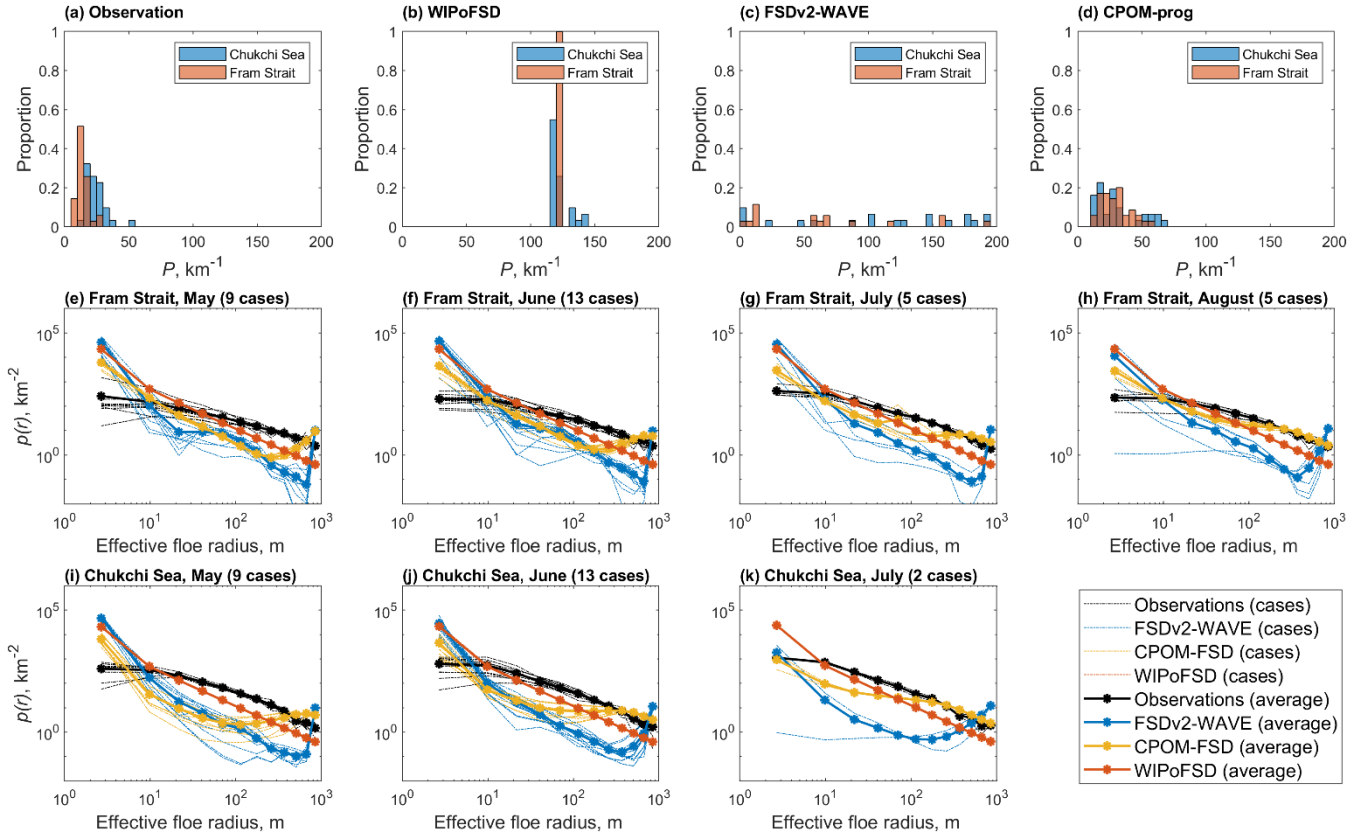

Figure S2. Frequency histograms of floe P from (a) observation, (b) WIPoFSD, (c) FSDv2-WAVE and (d) CPOM-FSD. In (a)–(d), blue colour indicates the frequency distribution of P for the Chukchi Sea and red colour for the Fram Strait. $p(r)$ are shown for (e) May, (f) June, (g) July and (h) August in Fram Strait, as well as for (i) May, (j) June and (k) July in the Chukchi Sea. In (e)–(k), the observations are shown in black line and three models in different colours (FSDv2-WAVE—blue, CPOM-FSD—yellow, WIPoFSD—red). In (e)–(k), dash lines correspond to the frequency distribution of $p(r)$ of individual cases in each month and solid lines are the mean of them. This figure is similar to Fig. 2 in the main text, but study area selected for models is a 5×5 grid-cells area containing the observational study regions.

Table S1. Difference in $p(r)$ (km^{-1}) of small floes integrated in floe size category 1 and 2 (r <14.29 m) between models and observations in the Chukchi Sea region and the Fram Strait region.

	FSDV2-WAVE		CPOM-FSD		WIPOFSD	
	CS[a]	FS[b]	CS	FS	CS	FS
May	151.57	218.95	52.46	83.41	108.76	124.76
June	129.65	211.29	53.25	49.21	107.38	125.99
July	57.60	108.86	38.95	20.60	106.41	129.68
August	/	33.94	/	20.42	/	146.07
Mean	112.94	143.26	48.22	43.41	107.52	131.62

[a] Chukchi Sea.

[b] Fram Strait.

Table S2. Summary of high-resolution optical satellite imagery used in this study, including satellite images provided by Measurements of Earth Data for Environmental Analysis (MEDEA) group (Kwok and Untersteiner, 2011; Kwok, 2014), WorldView-1 (WV1, Satellite Imaging Corporation, https://www.satimagingcorp.com/satellite-sensors/worldview-1/, last access: 16 February 2023) and WorldView-2 (WV2, Satellite Imaging Corporation, https://www.satimagingcorp.com/satellite-sensors/worldview-2/, last access: 16 February 2023). δ is the resolution of the satellite images. d_{min} is the lower bound of floes following the power law. p-value is of KS goodness-of-fit test.

Image name and date	Image type	δ (m)	Location	Cut image size (pixel)	d_{min} (m)	α	p-value
chukchi_20060517	MEDEA	1	70°N, 170°W	10675×11916	35	2.11	0
chukchi_20060603	MEDEA	1	70°N, 170°W	5024×10832	100	2.30	0.110
chukchi_20060604	MEDEA	1	70°N, 170°W	13486×17557	173	2.54	0.627
chukchi_20060612	MEDEA	1	70°N, 170°W	14048×12704	36	2.23	0
chukchi_20070610	MEDEA	1	70°N, 170°W	11728×7360	43	2.29	0.159
chukchi_20080612	MEDEA	1	70°N, 170°W	13632×14112	161	2.57	0.097
chukchi_20090601	MEDEA	1	70°N, 170°W	7136×4832	100	2.34	0.470
chukchi_20090608_cut1	MEDEA	1	70°N, 170°W	9152×7328	118	2.64	0.490
chukchi_20090608_cut2	MEDEA	1	70°N, 170°W	6000×6408	35	2.76	0
chukchi_20100527	MEDEA	1	70°N, 170°W	5236×5736	116	2.59	0.120
chukchi_20100530_cut1	MEDEA	1	70°N, 170°W	7632×8544	35	2.14	0.002
chukchi_20100530_cut2	MEDEA	1	70°N, 170°W	7080×10944	165	2.68	0.014
chukchi_20110529	MEDEA	1	70°N, 170°W	12192×8256	64	2.31	0.001
chukchi_20120601	MEDEA	1	70°N, 170°W	8557×9799	238	2.72	0.210
chukchi_20130509	MEDEA	1	70°N, 170°W	16416×13104	136	2.44	0.014
chukchi_20130531	MEDEA	1	70°N, 170°W	12736×5168	50	2.36	0.141
chukchi_20130601_WV2	WV2	0.54	71.5°N, 169.5°W	20556×10439	33	2.39	0.906
chukchi_20130610_cut1	MEDEA	1	70°N, 170°W	8352×12960	311	3.45	0.722
chukchi_20130610_cut2	MEDEA	1	70°N, 170°W	4248×10176	193	3.07	0.929

chukchi_20130617	MEDEA	1	70°N, 170°W	12480×10512	193	2.88	0.200
chukchi_20130707_WV2	WV2	0.47	72.6°N, 168.7°W	13992×11160	18	2.23	0.001
chukchi_20140502	MEDEA	1	70°N, 170°W	13504×12672	105	2.48	0.133
chukchi_20140513	MEDEA	1	70°N, 170°W	16656×12096	147	2.57	0
chukchi_20140527_cut1	MEDEA	1	70°N, 170°W	15616×4640	101	2.53	0.460
chukchi_20140527_cut2	MEDEA	1	70°N, 170°W	16000×2464	36	2.20	0.185
chukchi_20140610_cut1	MEDEA	1	70°N, 170°W	13008×6144	257	3.04	0.600
chukchi_20140610_cut2	MEDEA	1	70°N, 170°W	12912×5520	114	2.52	0.110
chukchi_20140623	MEDEA	1	70°N, 170°W	6928×6480	185	2.54	0.430
chukchi_20140624_WV2	WV2	0.58	72.6°N, 168.7°W	13248×11616	20	2.36	0.273
chukchi_20140707_cut1	MEDEA	1	70°N, 170°W	12976×3552	111	2.42	0.310
chukchi_20140707_cut2	MEDEA	1	70°N, 170°W	12928×2368	55	2.50	0.904
chukchi_20140707_cut3	MEDEA	1	70°N, 170°W	12848×2176	48	2.29	0.758
fram_20000607	MEDEA	1	84.9°N, 0.1°E	14472×12552	42	2.03	0.653
fram_20010606	MEDEA	1	84.9°N, 0.1°E	12768×8256	104	2	0.131
fram_20010611	MEDEA	1	84.9°N, 0.1°E	16008×8616	402	2.49	0.460
fram_20010615	MEDEA	1	84.9°N, 0.1°E	16416×7440	38	1.98	0.226
fram_20010624	MEDEA	1	84.9°N, 0.1°E	8212×12946	160	2.31	0.420
fram_20010630_cut1	MEDEA	1	84.9°N, 0.1°E	7640×8924	64	2.29	0.119
fram_20010630_cut2	MEDEA	1	84.9°N, 0.1°E	6448×7440	168	2.77	0.378
fram_20020608_cut1	MEDEA	1	84.9°N, 0.1°E	9728×7392	148	2.25	0.190
fram_20020608_cut2	MEDEA	1	84.9°N, 0.1°E	12672×6176	36	2.12	0.113
fram_20060613	MEDEA	1	84.9°N, 0.1°E	13200×12672	756	2.91	0.260
fram_20060719	MEDEA	1	84.9°N, 0.1°E	12928×9952	387	2.97	0.990
fram_20060803	MEDEA	1	84.9°N, 0.1°E	15712×8960	227	2.38	0.290

fram_20060810	MEDEA	1	84.9°N, 0.1°E	10848×9344	175	2.45	0.350
fram_20060825	MEDEA	1	84.9°N, 0.1°E	7536×5856	199	2.38	0.270
fram_20070511	MEDEA	1	84.9°N, 0.1°E	14560×10816	36	1.72	0.065
fram_20090501	MEDEA	1	84.9°N, 0.1°E	12544×12128	150	2.42	0.752
fram_20090602	MEDEA	1	84.9°N, 0.1°E	11486×11486	192	2.53	0.682
fram_20090703	MEDEA	1	84.9°N, 0.1°E	13248×10192	39	2.34	0.000
fram_20090804	MEDEA	1	84.9°N, 0.1°E	12888×9024	143	2.52	0.402
fram_20100629_cut1	MEDEA	1	84.9°N, 0.1°E	10032×8448	34	2.15	0.634
fram_20100629_cut2	MEDEA	1	84.9°N, 0.1°E	10608×5040	30	2.05	0.148
fram_20100820	MEDEA	1	84.9°N, 0.1°E	9528×10944	252	2.78	0.877
fram_20120519	MEDEA	1	84.9°N, 0.1°E	10912×6656	147	1.93	0.120
fram_20120625	MEDEA	1	84.9°N, 0.1°E	12885×12721	35	2.19	0.000
fram_20120728	MEDEA	1	84.9°N, 0.1°E	14712×11088	212	2.45	0.215
fram_20130510	MEDEA	1	84.9°N, 0.1°E	9216×5920	458	2.66	0.140
fram_20130520	MEDEA	1	84.9°N, 0.1°E	14144×9152	388	2.42	0.570
fram_20130524_WV1	WV1	0.52	76°N, 14°W	14016×11280	18	2.19	0.372
fram_20130528	MEDEA	1	84.9°N, 0.1°E	11872×5792	317	2.23	0.120
fram_20130605	MEDEA	1	84.9°N, 0.1°E	10976×9696	364	2.58	0.760
fram_20130605_WV2	WV2	0.59	84.9°N, 0.1°E	16776×14256	18	1.98	0.263
fram_20130618	MEDEA	1	84.9°N, 0.1°E	10608×10584	240	2.68	0.520
fram_20130720	MEDEA	1	84.9°N, 0.1°E	13120×12480	36	2.14	0.000
fram_20140505	MEDEA	1	84.9°N, 0.1°E	10656×16512	197	2.32	0.333
fram_20140516	MEDEA	1	84.9°N, 0.1°E	12720×18000	92	1.96	0.380
fram_20140707	MEDEA	1	84.9°N, 0.1°E	12388×13343	294	2.38	0.830

Table S3. Mean and standard deviation of the modelling P (km km^{-2}) of in the study regions of the Chukchi Sea (CS) and the Fram Strait (FS) shown in Fig. 1a in the main text and in a 5×5 grid cells containing the locations of observations.

	FSDV2-WAVE		**CPOM-FSD**		**WIPOFSD**	
	CS[a]	**FS[b]**	**CS**	**FS**	**CS**	**FS**
Original regions	136.95±70.58	178.36±89.28	59.55±19.13	61.19±28.95	120.93±1.66	138.99±12.98
5x5 grid cells	168.09±98.66	195.02±131.37	30.31±17.18	29.57±10.86	123.25±7.06	122.40±0.00

References

Bateson, A. W., Feltham, D. L., Schröder, D., Hosekova, L., Ridley, J. K., and Aksenov, Y.: Impact of sea ice floe size distribution on seasonal fragmentation and melt of Arctic sea ice, Cryosph., 14, 403–428, https://doi.org/10.5194/tc-14-403-2020, 2020.

Bateson, A. W., Feltham, D. L., Schröder, D., Wang, Y., Hwang, B., Ridley, J. K., and Aksenov, Y.: Sea ice floe size: its impact on pan-Arctic and local ice mass and required model complexity, Cryosph., 16, 2565–2593, https://doi.org/10.5194/tc-16-2565-2022, 2022.

Kwok, R. and Untersteiner, N.: New High-Resolution Images of Summer Arctic Sea Ice, Eos, Trans. Am. Geophys. Union, 92, 53–54, https://doi.org/10.1029/2011EO070002, 2011.

Kwok, R.: Declassified high-resolution visible imagery for Arctic sea ice investigations: An overview, Remote Sens. Environ., 142, 44–56, https://doi.org/10.1016/j.rse.2013.11.015, 2014.

Perovich, D. K.: Aerial observations of the evolution of ice surface conditions during summer, J. Geophys. Res., 107, 8048, https://doi.org/10.1029/2000JC000449, 2002.

Perovich, D. K. and Jones, K. F.: The seasonal evolution of sea ice floe size distribution, J. Geophys. Res. Ocean., 119, 8767–8777, https://doi.org/10.1002/2014JC010136, 2014.

Roach, L. A., Horvat, C., Dean, S. M., and Bitz, C. M.: An Emergent Sea Ice Floe Size Distribution in a Global Coupled Ocean-Sea Ice Model, J. Geophys. Res. Ocean., 123, 4322–4337, https://doi.org/10.1029/2017JC013692, 2018a.

Satellite Imaging Corporation, WorldView-1 Satellite Sensor: WorldView-1 Satellite Image, https://www.satimagingcorp.com/satellite-sensors/worldview-1/, last access: 16 February 2023.

Satellite Imaging Corporation, WorldView-2 Satellite Sensor: WorldView-2 Satellite Image, https://www.satimagingcorp.com/satellite-sensors/worldview-2/, last access: 16 February 2023.

Horvat, C. and Tziperman, E.: A prognostic model of the sea-ice floe size and thickness distribution, 9, 2119–2134, https://doi.org/10.5194/tc-9-2119-2015, 2015.